

Revealing the Nature of Melt Pool Boundaries in Additively Manufactured Stainless Steel by Nano-Sized Modulation

Konstantin Sommer,* Leonardo Agudo Jácome,* René Hesse, and Dirk Bettge

In the current study, the 3D nature of the melt pool boundaries (MPBs) in a 316 L austenitic steel additively manufactured by laser-based powder bed fusion (L-PBF) is investigated. The change of the cell growth direction and its relationship to the MPBs is investigated by transmission electron microscopy. A hitherto unreported modulated substructure with a periodicity of 21 nm is further discovered within the cell cores of the cellular substructure, which results from a partial transformation of the austenite, which is induced by a Ga⁺ focused ion beam. While the cell cores show the modulated substructure, cell boundaries do not. The diffraction pattern of the modulated substructure is exploited to show a thickness ≥ 200 nm for the MPB. At MPBs, the cell walls are suppressed, leading to continuously connecting cell cores across the MPB. This continuous MPB is described either as overlapping regions of cells of different growing directions when a new melt pool solidifies or as a narrow planar growth preceding the new melt pool.

between the freshly solidified melt pool and the existing solid material it was built on during one melting pass. This microstructural feature has a characteristic morphology and under some circumstances can be revealed by polishing and etching a metallographic section, that is, it is prone to selective corrosion.

Micrographs of such etched cross sections have been presented manifold in past works, for example, Figure 1a,b of Avila et al.,^[9] which respectively show micrographs of such etched cross and longitudinal sections of the same material state studied here. In the case of their Figure 1b, the image plane is parallel to the building direction (BD = Z), as shown by the black arrow in the bottom left of the image. The etched MPBs appear as dark lines in optical images as highlighted there.

From such micrographs, it is not clear if the MPB has a structure itself, which is then preferentially etched, or if it is just the boundary between adjacent melt pools without a distinct microstructure of its own. The morphology of the MPB depends on L-PBF process parameters such as laser power and scanning speed.^[8] In multilayer manufacturing, the MPBs in such sections provide information on the scanning strategy that was used to build the structure. In the example given by Avila et al. in their Figure 1b, where the BD is orientated vertically, the shape and position of the MPBs arise from the positions and directions of the laser paths that are parallel to X and Y, the plane perpendicular to the BD, in this specific example.

In most cases, the MPBs are found to be single lines in the cross section (as indicated by the example in Avila et al.^[9]), while occasionally appearing as multiple lines, as noted by Godec et al.^[10] The MPB defines the region of the heat-affected zones (HAZs)^[11] in the building plate for the first layers, or previously deposited layers for subsequent layers. In LPBF and other AM processes where epitaxial grain growth occurs, the MPB also defines the size and position of grains at the start of solidification of a melt pool. This is followed by competitive growth of grains affected by crystallographic orientation and thermal gradients.^[12–14]


Metallic materials produced by LPBF typically display a fine cellular substructure within the grains, whereby the cells exhibit sizes from submicron to a few microns.^[15,16] The cell structure consists of long columnar regions that are separated by a fine interconnected network of surrounding material (cell walls) with a higher dislocation density than within the cell interior.^[10] According to Kou,^[17] the cellular structure is formed due to

1. Introduction

Additive manufacturing (AM) has become relevant for many industrial sectors due to its very flexible layer-by-layer construction principle, making the production of geometrically complex parts possible.^[1] However, the widespread usage of AM technologies is currently constrained by its costs.^[2] To overcome the limitations, the AM processes must be optimized and accelerated, which requires a detailed understanding of the effects of manufacturing strategies on the microstructure of the material and its consequent properties.

Laser-based powder bed fusion (L-PBF) is the most widely used technology for AM of metallic alloys. During the L-PBF process, the workpiece is built up via melting successive powder layers with a laser.^[3–5] The melt pool boundary (MPB), also known for example as fusion line,^[6–8] is the interface that arises

K. Sommer, L. Agudo Jácome, R. Hesse, D. Bettge
Department 5: Materials Engineering
Bundesanstalt für Materialforschung und -prüfung (BAM)
Unter den Eichen 87, 12205 Berlin, Germany
E-mail: konstantin.sommer@bam.de; leonardo.agudo@bam.de

 The ORCID identification number(s) for the author(s) of this article can be found under <https://doi.org/10.1002/adem.202101699>.

© 2022 The Authors. Advanced Engineering Materials published by Wiley-VCH GmbH. This is an open access article under the terms of the Creative Commons Attribution License, which permits use, distribution and reproduction in any medium, provided the original work is properly cited.

DOI: 10.1002/adem.202101699

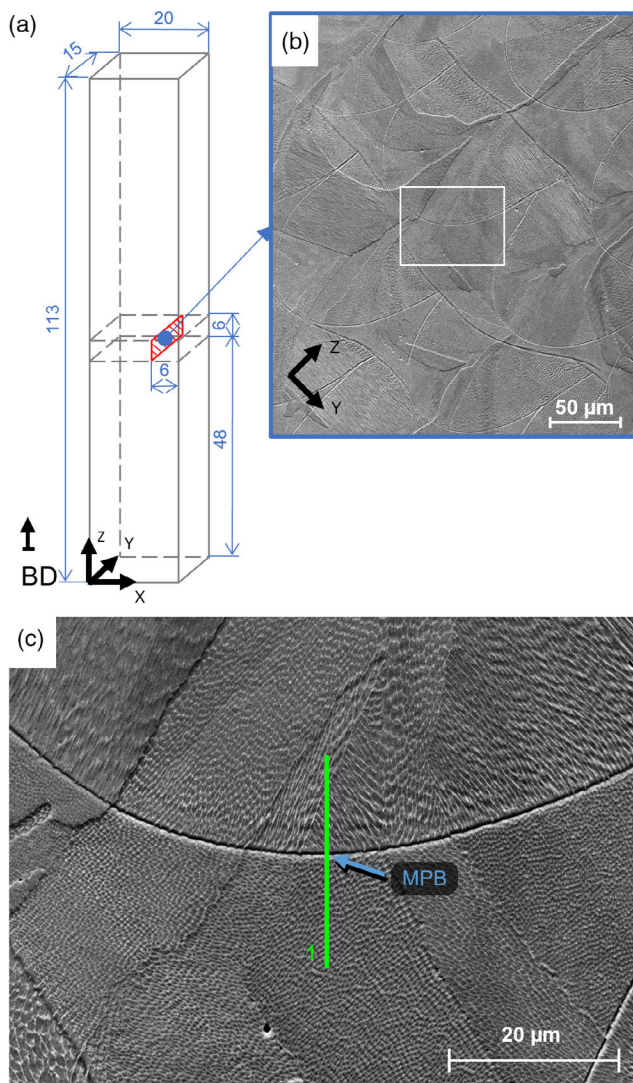


Figure 1. Sample preparation and microstructure: a) morphology of laser-based powder bed fusion (L-PBF) 316 L built prism and investigated section position (red); b) typical secondary electron scanning electron microscopy (SE-SEM) image showing the L-PBF 316 L microstructure (45° rotated clockwise about X axis, compared to red rectangle in (a)); c) higher magnification of white rectangular region in (b) showing targeted preparation of the transmission electron microscope (TEM) lamella with positions of melt pool boundary (MPB, blue) and spatial reference “1” (green).

the cellular solidification mode, as characterized by high-temperature gradients and growth rates. Due to the high cooling rates during solidification in L-PBF, the cellular structure grows along a direction that is dominated by the thermal gradient, where the crystal orientation with the lowest energy for solidification has the highest solidification velocity.^[18] For face-centered cubic (FCC) and body-centered cubic (BCC) crystalline phases, the easiest growth directions are 100 .^[17] Some authors have successfully simulated the formation process of dendritic substructures during the L-PBF solidification process.^[19]

There are many detailed transmission electron microscopy (TEM) investigations of L-PBF 316 L features including secondary phases, grain boundaries, cells, dislocation networks, segregations, and precipitations.^[10,13,15,20–38] Barkia et al. reported the presence of a few stacking faults in the as-built 316 L L-PBF material next to the dislocation network at the cell wall, which gave an indication of its low stacking fault energy.^[22]

Some publications have reported the dimensions of MPBs or melt pool morphologic features such as depth and width to compare the microstructure of specimens produced with different process parameters.^[39] Godec et al. showed that the content of Cr, Mn, and Mo was lower both at MPBs of L-PBF 316 L and within the cell interior as compared to cell walls.^[10] Wang et al. observed a continuous feature $\approx 3 \mu\text{m}$ thick at MPBs of 316 L L-PBF and therefore assumed a change of solidification mode from planar to cellular to be responsible for this observation.^[15] A similar feature with a thickness $\approx 2 \mu\text{m}$ can be seen in micrographs by Krakhmalev et al.^[26] Pham et al. observed a continuous feature of $\approx 1 \mu\text{m}$ in thickness at some MPBs in the high entropy alloy (HEA) CrMnFeCoNi and explained it with the change of solidification mode.^[40] The continuous features reported before with a defined thickness at MPBs were imaged using scanning electron microscopy (SEM) on etched cross sections. These features are visible in SEM micrographs following etching. However, the influence of etching on the morphology is unclear.

Furthermore, many metallic AM materials exhibit characteristic microstructural features at or near MPBs. For example, in AlSi10Mg manufactured with L-PBF, coarse cellular dendrites were found in the region above MPB, while fine cellular dendrites are observed in the middle of melt pool.^[41] Equiaxed grains were observed next to MPBs of L-PBF alloys AlMgScZr and IN718.^[42,43] Vrancken et al. reported the presence of microsegregation of alloying elements at MPBs for L-PBF Ti6Al4V and a derivate alloy.^[44] However, L-PBF 316 L lacks such distinctive microstructural features around the MPB, which subsequently make it difficult to define its boundaries.

The aim of this work is therefore to elucidate in detail the microstructural characteristics that define MPBs in 316 L L-PBF through the targeted investigation with the use of correlative electron microscopy methods. In particular, we aim to understand the crystallographic and morphological structure of the MPB without the effect of surface etching.

2. Experimental Section

2.1. Material

The investigation was performed on austenitic stainless steel 316 L manufactured by L-PBF. The feedstock powder used had a mean particle diameter of $d_{50} = 23 \mu\text{m}$ and was atomized with nitrogen gas. **Table 1** shows the chemical composition of manufactured samples as previously reported, measured using combustion/infrared-detection, carrier gas hot extraction, X-Ray fluorescence spectrometry (XRF), and inductively coupled plasma optical emission spectrometry (ICP-OES),^[45] which were compared to ASTM A276.^[46]

Table 1. Chemical composition of 316 L L-PBF^[45] as compared to ASTM A276.^[46]

| | | Chemical elements [wt%] | | | | | | | | | |
|----------------|------|-------------------------|-------|------|-------|-------|------|------|------|------|-------|
| | | Fe | C | Mn | P | S | Si | Ni | Cr | Mo | N |
| ASTM A276 | Min. | Bal. | – | – | – | – | – | 10.0 | 16.0 | 2.00 | – |
| | Max. | Bal. | 0.030 | 2.00 | 0.045 | 0.030 | 1.00 | 14.0 | 18.0 | 3.00 | – |
| L-PBF material | | Bal. | 0.016 | 0.90 | 0.009 | 0.004 | 0.52 | 12.9 | 18.0 | 2.42 | 0.078 |

2.2. L-PBF and Heat Treatment

The L-PBF process was performed on a commercial L-PBF single laser system SLM280HL (SLM Solutions Group AG, Lübeck, Germany) using the parameters in **Table 2**. During the process, 18 prism samples with a rectangular base and dimensions $114.5 \times 20.0 \times 13.0 \text{ mm}^3$ (H \times W \times D) were manufactured on the base plate. The height (H) of the samples was oriented along the BD such that the BD was 90° to the build plate. The adjacent hatches within one layer were parallel to each other but alternate in their directions. The hatches of different layers were oriented parallel to one of the sample edges and were rotated 90° from one layer to the next layer. After manufacturing, the samples were subjected to a stress-relief heat treatment at 450°C for 4 h and sawed from the base plate (final height: 113 mm, Figure 1a). The heat treatment was performed in argon, after which the samples were cooled inside the furnace.

2.3. Sample Preparation

To investigate the MPBs, a longitudinal section was prepared from one of the prisms. Earlier investigations on such prisms, manufactured with the same parameters, showed nearly the same size distribution for the grain and cellular structures for the top and bottom regions of the samples.^[39,45] Figure 1 shows the steps taken for sample preparation. In Figure 1a, a schematic representation of the rectangular prism is shown, where the dimensions (in millimeter) are marked, and the sample reference system is drawn at the bottom left, with BD \parallel Z. To investigate the nature of MPBs, a section parallel to the plane YZ was extracted from within the sample (red region in Figure 1a) using SiC cutting discs and subsequently prepared by grinding with emery papers of 180, 320, 600, and 1200 grit and polishing with suspensions of 3 and $1 \mu\text{m}$ diamond particles. For electron back-scattered diffraction (EBSD), as well as for targeted preparation of the TEM lamella, the sections were finally electropolished on a Lectropol-5 device (Struers GmbH, Willich, Germany) using the Struers electrolyte A2 at 30 kV for 40 s.

Although electropolishing was not as strong as chemical etching, a topography was still created at locations where crystal

defects or chemical heterogeneities affected the reactivity with the electrolyte. Thus, MPBs appeared as thick dark/bright lines that are targeted to ensure the subsequent extraction of electron-transparent TEM lamellae from these locations. Figure 1b shows a secondary electron (SE-)SEM image of an electropolished sample. The region shown in Figure 1b is equivalent to the OM image of the etched sample in Figure 1b of Avila et al.^[9] but it is presented here at a higher magnification on the YZ plane and rotated 45° clockwise around the X axis. (Note the rotation of the coordinate systems in Figure 1a,b).

The region within the white rectangle in Figure 1b is shown at a higher magnification in the SE-SEM in Figure 1c. The position that crosses an MPB, where the TEM lamella was extracted by means of a focused ion beam (FIB), is marked by the vertical green line. The location of the MPB on the lamella is marked with a blue arrow on Figure 1c. The lamella was prepared in a FEI Quanta 3D Dual Beam FIB (FEI Company, now Thermo Fisher Scientific, Hillsboro, Oregon, USA) at an acceleration voltage of 30 kV for the Ga^+ ion beam, using the Omniprobe in situ lift-out system (Oxford Instruments plc, Tubney Woods, Abingdon, UK).

2.4. Microscopy

The SEM, which included EBSD measurements, was conducted using a Leo Gemini 1530 VP SEM (Leo Electron Microscopy Inc., New York, USA) equipped with a high-resolution EBSD detector e-FlashHR+ (Bruker Corporation, Billerica, USA), which has an attached forescattered electrons (FSEs) detector. The software package ESPRIT 1.94 (Bruker Corporation, Billerica, USA) was used for acquisition, indexing and post-processing of EBSD data. The images were acquired at an acceleration voltage of 20 keV. EBSD and FSE imaging was performed at a sample tilt of 70° , a pixel size of 100 nm, and 10 nA beam current.

The TEM analysis was performed on a JEOL JEM-2200FS (JEOL Ltd., Tokyo, Japan) at an acceleration voltage of 200 kV. The built-in omega-type energy filter (EF) was used for zero-loss EF selected area diffraction (SAD), as well as bright-field (BF) and dark-field (DF) conventional (C) TEM imaging, which was implemented to correlate crystallographic and morphologic features of

Table 2. L-PBF process parameters.

| Parameter | Protective gas | Laser Power [W] | Layer thickness [mm] | Hatch distance [mm] | Scanning speed [$\text{mm}\cdot\text{s}^{-1}$] | Base plate temperature [$^\circ\text{C}$] | Laser spot diameter [mm] |
|-------------------|----------------|-----------------|----------------------|---------------------|--|---|--------------------------|
| Value/description | Argon | 275 | 0.05 | 0.12 | 700 | 100 | ≈ 0.08 |

the cellular substructure. Energy-dispersive X-Ray spectrometry (EDX, JEOL JED-2300 detector; JEOL Ltd., Tokyo, Japan) was implemented in high angle annular dark field (HAADF) scanning (S) TEM for point analysis where needed.

3. Results

First, the problematic of the relationship between cellular morphology and MPBs (Figure 2a,b) with respect to crystal orientation (Figure 2c–g) is reported for the present material. Figure 2a shows the FSE image of an electrolytically etched longitudinal section oriented parallel to BD and parallel to the sample edge, that is, on the plane parallel to YZ (see Figure 2a).

Figure 2b is a magnified micrograph of the region marked with a white rectangle in Figure 2a. Due to electropolishing-related topography effects in these SEM images and the shadowing effect of the FSEs at the high sample tilt of 70°, many features of the microstructure can be clearly observed. MPBs are apparent as approximately curved lines that extend over several tens of

microns. For example, the white rectangle in Figure 2a is located at a triple point arising from two perpendicular MPBs. The cellular substructure is apparent throughout the cross section, see Figure 2b. The structures on the cross section that are consistent with the cells have a columnar morphology. In cases where cells are cut at an angle $<45^\circ$ to their growth direction (e.g., lower right quadrant of Figure 2b), a honeycomb-like structure is obtained (cf. vertically cells delineated in red). In cases where the growth direction of the cells is nearly parallel to the sectioning plane (lower left quadrant of Figure 2b), a lamellar structure can be seen (cf. red lines almost aligned with Y direction).

The $\{100\}$ pole figure in Figure 2c shows three narrow point clouds. Two of these point clouds are found almost on the trace of the Y plane, somewhat halfway between X and Z directions (at $\approx 45^\circ$ from either direction), which explains the green color within the white rectangle on the respective IPF in Figure 2e,g. The third point cloud is located on the left of Figure 2c, almost on the great circle and only 4° from the Y direction. A red line pointing at the latter set of points matches the growth direction of cells of the on bottom left of Figure 2b.

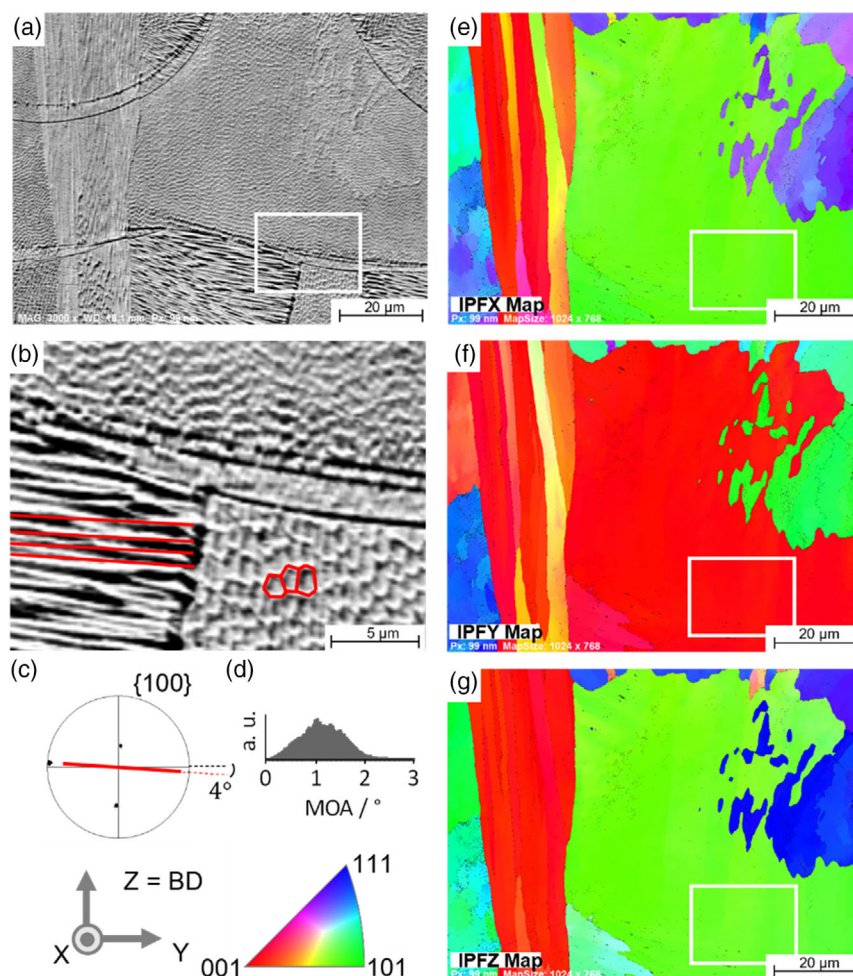


Figure 2. Electropolished section of L-PBF 316 L. a) Forescattered electrons (FSEs) micrograph revealing cellular structures. White square denotes region to which (b–d) refer. b) Detail of (a) with schematic of cellular structure in red. c) $\{100\}$ pole figure for orientations found in (b), along with d) misorientation average (MOA) histogram. e–g) Inverse pole figure (IPF) maps along e) X, f) Y, and g) Z of region shown in (a). A color-coded IPF triangle and the sample reference coordinate system are shown in the bottom left. For details, see Section 3.

The inverse pole figure (IPF) maps (Figure 2e–g) of the region in Figure 2a do not display any change of crystallographic orientation at the MPBs, although the growth orientation of cellular structures clearly alters. The IPFs show consistently that there are no discernable differences in the crystal orientation in the region shown in Figure 2b (marked in the IPFs of Figure 2e–g with a white rectangle), even if the morphology of the cells is markedly different on either side of the MPBs. To illustrate this narrow orientation spread, Figure 2d shows the misorientation average (MOA) histogram, in which a comparison of all orientations found in Figure 2b display $\approx 1^\circ$ misorientation angle with respect to the average orientation in that region. In Figure 2a, some cell structures have also grown in BD

and thereby have crossed multiple MPBs without changing their crystallographic orientation. The very large grain in the center of the image is also observed to cross several MPBs.

Considering this microstructure, the FIB lamella was extracted at another location similar to that of Figure 2b, that is, at an MPB with changing cell growth directions within one grain, as marked by the green vertical line in Figure 2c. The lamella was then investigated by SAD and dark field (DF) TEM (DFTEM), as shown in Figure 3a and 4, as well as by EDX (Figure 5). In Figure 3a, a montage of eleven DFTEM images is shown, the contrast of which arises by selecting the region marked by a blue circle (“DF1”) on the SAD pattern at the bottom right to induce the DFTEM contrast. In turn, this

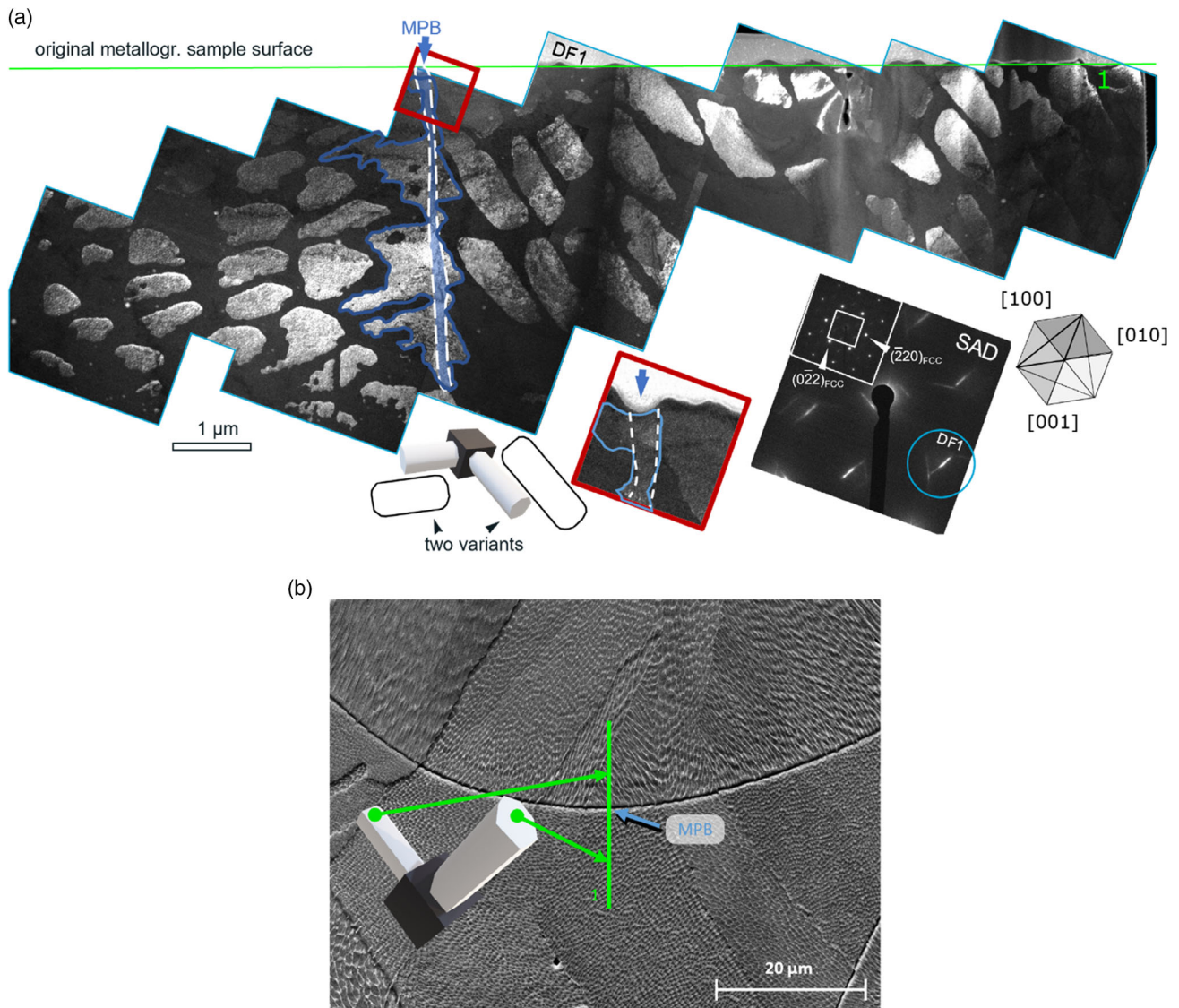


Figure 3. a) Montage of dark-field TEM (DFTEM) micrographs (top) with associated selected area diffraction (SAD) pattern (bottom right). Schematically, the original sample surface (see Figure 2c) has been marked with a straight green line as in (b). MPB is highlighted by the semitransparent blue region surrounded with a dotted white line. The older melt pool is on the right side in this image, the newer one is seen on the left side (cf. green “1” marked here on the right, and on the bottom of (b)). b) SE-SEM image as in Figure 2b. Black 3D cubic lattice cell with the crystal orientation at the MPB region, where idealized cell morphology (bright cylinders with polygonal base) matches projected cell growth directions, is shown in a) TEM and b) SEM (for details, see Section 4).

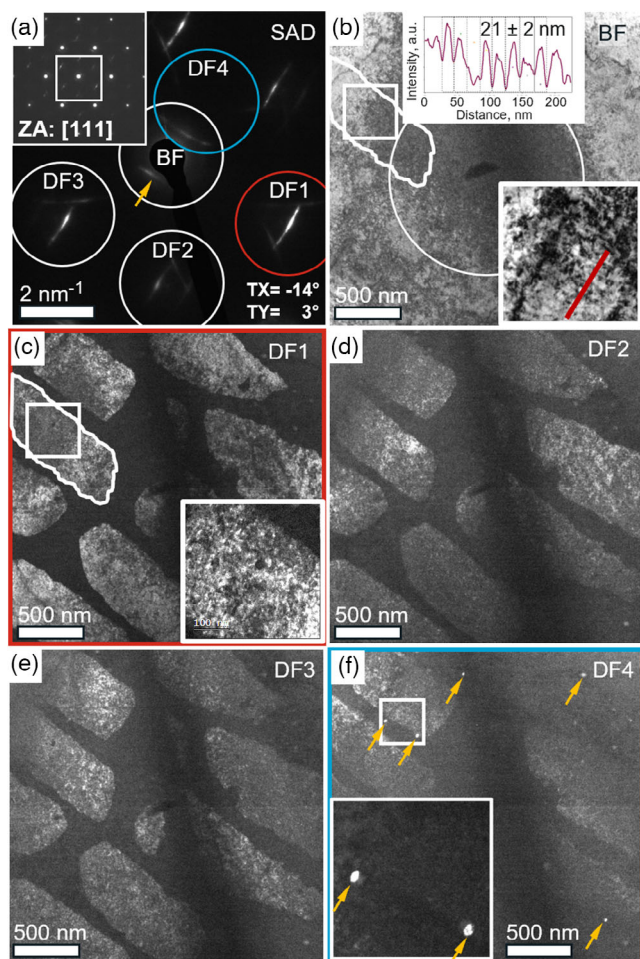


Figure 4. Bright-field (BF)/DF-TEM image series from different regions of SAD pattern detail. Streaks appearing at three $\approx 1/3\{112\}$ locations give rise to DF-TEM images DF1, DF2, and DF3, where mostly cells contribute to image formation. The DFTEM image DF4, associated with positioning the objective aperture at the $\approx 1/3(01\bar{1})$ reflection (blue circle on top left) mostly shows small elongated $\text{Si}_x\text{Mn}_y\text{O}_z$ nanoparticles (yellow arrows on DF4). (For details, see text.)

SAD pattern was acquired from the central region of the montage marked with a white circle. The latter SAD pattern was acquired at a large camera length, so as to avoid the strong $\{110\}_{\text{FCC}}$ reflections and enhance the faint intensities at smaller diffraction vectors (a similar SAD pattern with the indexed $\{110\}_{\text{FCC}}$ reflections is found in Figure 4a). The inset in this SAD shows another SAD at a lower camera length, which reveals the threefold symmetry of the main austenitic reflections imaged in the zone axis ($\text{ZA} = [111]$). In the inset SAD pattern, a white square is inscribed to demark the region from which the enlarged SAD was acquired; note that the main $\{110\}_{\text{FCC}}$ reflections are not present in the enlarged SAD pattern. In this enlargement, a series of streaks elongated in directions approximately orthogonal to $(10\bar{1})_{\text{FCC}}$, $(\bar{1}\bar{1}0)_{\text{FCC}}$, and $(0\bar{1}\bar{1})_{\text{FCC}}$ are present with the latter being strongest (see schematic lattice with inscribed indexes on its left). A closer view reveals a curvilinear path with an angular variation of up to $\approx 10^\circ$, as measured on the streak with the strongest intensity

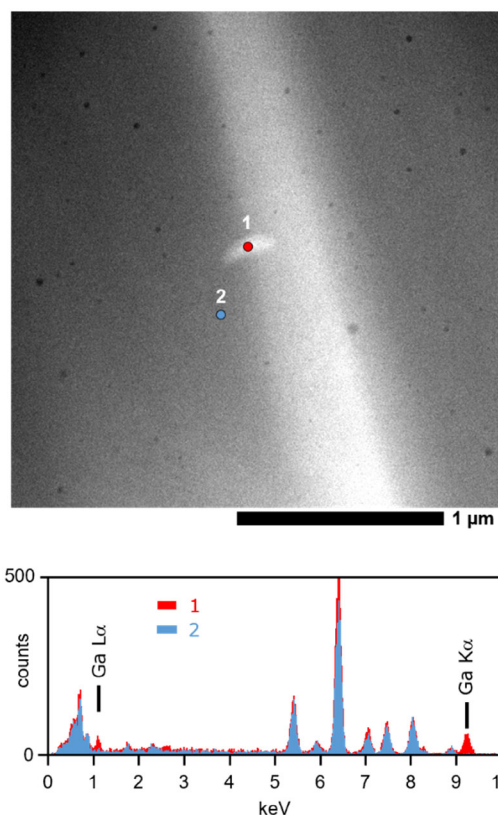


Figure 5. High angle annular dark field (HAADF) scanning (S)TEM image (top) and overlapped energy-dispersive X-Ray spectra (EDS) of points 1 and 2, marked on HAADF STEM image.

profile. However, the average deviation from the aforementioned plane normals is of $\approx 2^\circ$ (compare with the schematic orthogonally projected lattice cell in gray at the bottom of Figure 3a, where the directions 100 and 110 are drawn).

The straight continuous horizontal green line drawn above the montage of DF images in Figure 3a denotes the idealized position of the surface of the metallographic sample from where the FIB lamella was extracted (cf. Figure 3b). Although this position is idealized as a straight line, a certain topography is present due to the original weak etching effect of the electropolished sample. A continuous blue line that departs at the intersection of the metallographic sample surface and the MPB position (highlighted in blue), delineates the only uninterrupted cell/wall interface found to extend from the surface over $4\ \mu\text{m}$ downward, that is, into the depth of the region in the original metallographic sample surface. The remaining cells appear as isolated islands, the longest of which reaches about $1\ \mu\text{m}$ in depth from the original metallographic sample surface (on the right side of the MPB).

To highlight the MPB, a semitransparent blue elongated area with a dotted white line has been overlaid onto the continuous blue line. This area highlights a straighter region in which the thickness of the MPB is determined by the thinnest links within the continuous blue line. Note that on either side of this dotted white line, facets tend to adopt those from discrete cells (schematically drawn under the MPB). On the left of this dotted white

line, the cells were cut such that their main growth axis seems more horizontal on the image, whereas cells on the right appear more vertical. These facets are schematically presented by the two white rectangles at the bottom of Figure 3a as two cell “variants.” In turn these variants of the elongated cells that form during L-PBF are represented by two schematic 3D cell cylinders that emerge with an idealized polygonal cross section, and with their growth direction parallel to $[100]$ and $[010]$ of the 3D black cubic lattice. This 3D cube represents the FCC crystal orientation of the austenite. Knowing the relative rotations between the lamella imaged in Figure 3a and the original metallographic sample surface of Figure 1c, the 3D model has been rotated back to match the latter SE-SEM image, as presented in Figure 3b. The blue MPB and the green “1” marked on the right of the montage in Figure 3a correspond to the annotations on Figure 1c and 3b (original surface of the metallographic sample).

The region under the depression of the original metallographic surface at the MPB is marked by a tilted red square and enlarged in the inset DFTEM image between the montage and the diffraction pattern of Figure 3a. Here, the depression seems clearer (marked with a light blue arrow) as compared to other protuberances from the contour of the electropolished sample.

The characteristics of both sides of the MPB were also analyzed via SAD/DFTEM on regions that covered very similar features (not shown here). In the SAD patterns acquired from the corresponding regions, the main streaks orthogonal to $(10\bar{1})_{\text{FCC}}$ still show the strongest intensities. These streaks, as well as additional streaks close to the transmitted beam, orthogonal to $(2\bar{1}\bar{1})_{\text{FCC}}$, which do not contribute to the image, are addressed in Figure 4. A small region was identified that contained a ferritic phase along $ZA = [013]_{\text{BCC}}$. However, the ferritic region is not clear in the DFTEM images, as the ferritic reflections are excluded from the region of the SAD pattern that gives rise to the bright areas in the DFTEM images of Figure 3a.

Figure 4 shows a series of CTEM images acquired in the central region of Figure 3a, on the right side of the MPB, with the typical features as presented earlier. A SAD pattern acquired along $ZA = [111]$ is presented in Figure 4a, where the inset presents the short camera length (overview) region with the main austenitic reflections. The SAD pattern displays the characteristic streaks. The series of DFTEM images on the middle and bottom rows (Figure 4c–f), together with their BF counterpart in Figure 4b arise from the intensities within the objective apertures marking the different regions in the SAD pattern. Figure 4c–e corresponds to the regions marked DF1, DF2, and DF3 on Figure 4a. These DFTEM show that the same regions, the cell cores, are clearly observable due to the higher contrast when using the streaks roughly aligning along $(01\bar{1})$ (strongest intensities) and $(10\bar{1})$ and $(1\bar{1}0)$ (weaker intensities, cf. indexed SAD pattern and schematic lattice in Figure 3a).

Although they appear at different locations in the SAD pattern, all streaks contained in the circled regions DF1, DF2, and DF3 on the SAD pattern detail of Figure 4a can be associated to the cell cores. The streak that aligns parallel to $(01\bar{1})$ is strongest within the red circle marking DF1 in the SAD pattern. Looking closely inside of one of the cell cores, for example, as delineated in white in Figure 4c and thus identifying the corresponding location in

the BF image, one can observe a faint substructure in the latter, which aligns orthogonal to the streak. This substructure is more evident in the inset BF image, at the bottom of Figure 4a which is an enlargement of the region within the white square in the delineated cell. The red intensity profile inset on the top of Figure 4b, shows the boundaries of this substructure to be found every 21 ± 2 nm, and it stems from the straight red line on the inset BF at the bottom of Figure 4b. This intensity modulation could not be discerned in the corresponding DF1 enlargement (see inset at bottom right corner of Figure 4c).

Conversely, the strongest contrasts in Figure 4f (DF4) mostly arise from the streaks found to extend orthogonal to $(2\bar{1}\bar{1})_{\text{FCC}}$ within the blue circle in the SAD pattern (see yellow arrow in Figure 4a). These contrasts are found in the Figure 4f as bright dots (see yellow arrows), which present a projected oval shape with major and minor axes of ≈ 25 and 15 nm, respectively (see inset image, enlargement of white square in Figure 4f). A black trapezoidal particle ≈ 300 nm in width is present in the middle of the selected region. A high amount of Ga, the ion species used for thinning the sample to electron transparency, could be determined in the particle via energy-dispersive X-Ray spectroscopy (EDS point 1 in Figure 5), as compared to a region of uniform contrast (EDX point 2). However, this feature did not show diffraction contrast in any of the DFTEM images shown in Figure 4. The region displays brighter contrast in the DF scanning (S)TEM image in Figure 5, indicating a thicker or denser region. There are dark grey circular regions ranging from a few nanometers to some tens of nanometers also present. Due to its isolated appearance and apparent irrelevance for the objective of this work, it will not be further discussed.

4. Discussion

The influence of the 90° rotation angle of the scan strategy between passes of subsequent XY layers (compare coordinate system in Figure 2a) in the resulting microstructure is visible in the SE-SEM micrograph of the etched surface shown in Figure 2b. Within each layer (with a thickness of $\approx 50 \mu\text{m}$), a displacement is observed between the MPBs and the inverted arch-shaped grains, where the lowest points of the MPBs roughly coincide with the plane separating the grain columns. The whole region marked with a white rectangle in Figure 2a,e,g, corresponding to where the MPBs of two layers meet, displays a single crystal orientation with an orientation spread of $< 3^\circ$ (Figure 2d), with the IPF maps along all three reference axes showing uniform colors with roughly $Y \parallel [010]$, $X \parallel [101]$, and $Z \parallel [10\bar{1}]$. However, the enlargement in Figure 2b also shows that the MPB triple point is characterized by at least two, if not more, distinct growth morphologies of the characteristic cellular structure. Nonetheless, the resolution of the SEM is not sufficient to show these projections clearly, especially at the etched MPB with the associated material removal. Therefore, we used the TEM on an etch-free lamella to further resolve the morphology and structure of the MPB.

Figure 3a shows details around an MPB, where the crystal orientation of the grain on both sides also barely changes, but the cell structure growth direction is clearly different. With the knowledge of the crystallographic orientation from the

SAD pattern and the shapes of the cell structure on both sides of the MPB, a 3D model of the interpreted cell growth directions has been schematically illustrated within Figure 3a (bottom). The 3D model has been rotated to be superimposed on the original surface of the sample where the FIB lamella was extracted (lower left of Figure 3b). The cell structure projections of the corresponding figures in the TEM and SEM images are qualitatively in line with the 3D model of the cell structure morphology. The growth axis of these cell structures can then be compared to the macroscopic direction of the scan strategy (note the 45° rotation of images in Figure 2b,c).

It is well known that the solidification in 316 L tends to follow (100) directions provided that the heat flow is such that they can align with it during growth. The black part of the 3D drawing at the bottom of Figure 3a and the schematic grey drawing in addition to it depict the overall orientation of the crystal in the whole region of the montage. The morphology of the cell “islands” on the left and right of the MPB (e.g., schematic white rectangles on bottom of Figure 3a) is then explained by the section of the FIB lamella plane. This intersection follows the main axes parallel to the schematic 3D cylinders that emerge from the (100) and (010) faces of the black 3D cube as schematically shown at the bottom of Figure 3a.

In **Figure 6**, an interpretation of the steps that lead to such a configuration is presented schematically. Figure 6a first shows a macroscopic snapshot of several MPBs, which appear after the corresponding passes of the laser. In red, a liquid melt pool borders the non-molten powder bed on its top right (dark gray) and the surrounding solidified material. The laser moves in the direction of the black arrow. The region of the MPB at the lower right part of the schematic depicts where the liquid metal borders a subjacent solidified pass, which is orientated at 90° to the current pass. Figure 6b–d schematically illustrates the cellular structure interface at this MPB. In Figure 6b, the cell structure of the lower layer had solidified with its morphological axis orthogonal to the figure, and the new pass partially melts this structure. This view in Figure 6b is clearer than the oblique cut of the TEM lamella prepared for the analysis in Figure 3a.

According to Figure 3a, the continuous interface arising at the MPB between the cell cores and the cell walls can be attributed to a change in growth direction of the newly solidified cells on the left of the MPB seen in Figure 3a following the 90° rotation to the former layer. This event causes a change from a [100] growth

direction to a new [010] growth direction, which also form an angle of 90°, hence requiring minimal or no crystal rotation but only a morphological change. Such a mechanism is described by, for example, Chen et al.^[47] Thus, the newly solidified horizontally elongated cells that form in the new melt pool to the left of the MPB meet the formerly solidified cells (more vertically orientated on the right of the MPB in Figure 3a). The early stage of this process is depicted in Figure 6c in a simplified view, where a thin strip at the boundary depicted by with dotted lines indicates the start of epitaxial growth. However, the heat flow is orthogonal to the interface, which then controls the direction of solidification, as shown in Figure 6d. The schematic representations in Figure 6b–d derived from the experimental analyses thus show former cells that are orthogonal and newer ones are parallel to the figure plane. In Figure 3a, the junction of both morphologies at the MPB becomes coalesced cells that extend into the depth of the metallographic sample from which the FIB lamella was extracted. As all cell cores and the MPB present similar diffraction contrast in the DF image of Figure 3a, it seems reasonable to assume that there is no marked difference in their constitution, that is, in their chemical composition and structure.

The continuous structure marked in blue in Figure 3a seems to be only different in its morphology, compared to the isolated cell “islands” found on either side of the MPB, which could only be revealed by enhancing the cell cores thanks to their modulated nanostructure. Indeed, most of the TEM characterization performed herein made use of streaking effects found in the diffraction patterns. These effects are due to the nanometric modulation (see insets in Figure 4b) found in the cellular structure, which is retained throughout the FIB lamella. This feature of the cellular structure of L-PBF 316 L has to date not yet been reported, to the authors knowledge. Nonetheless, it is known that austenitic stainless steels are prone to a Ga⁺-induced ferritic transformation,^[48–52] mainly due to the stabilization of ferrite by Ga, but the extent of the transformed regions may also be affected by the strain induced during implantation.^[50] Knipling et al. concluded that the austenite composition is the most important factor controlling the Ga-induced transformation, while the second and third factor respectively being the beam dose and crystal orientation.^[48] In their detailed study where they irradiated 316 L stainless steel with 30 kV Ga⁺, Babu et al. stated that as little as 0.5% Ga by atom is enough

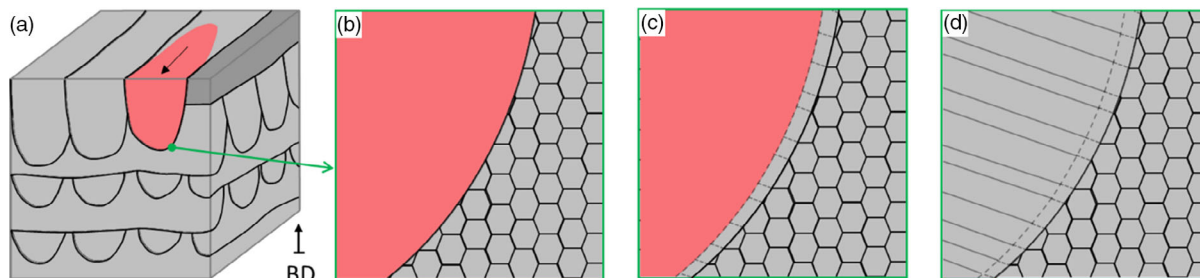


Figure 6. Schematic of proposed formation mechanism for MPB during L-PBF process. The MPB arrangement originates from layer-by-layer subsequently orthogonal passes, macroscopically shown in (a). Magnification of a) a new pass (in red) partially melts the b) cells of previous layers. The continuous MPB forms either by overlapping cells that change their growth direction or by planar solidification (c, compare dashed contours of MPB and cells). d) Newer cells solidify epitaxially from MPB, following thermal gradient.

to stabilize ferrite.^[50] They also show that different variants of ferrite may be triggered during the transformation. Additionally, depending on the crystal orientation of the parent FCC phase with respect to the incoming Ga⁺ beam, the triggered ferrite can be restrained to the location where sufficient Ga is chemically present or grow further (up to 120 nm) due to strain-induced ferritic transformation associated to ion implantation. The latter was observed in their work on samples where the parent FCC grain normal orientation was parallel to [122], an orientation that also is very close to the foil normal n ($= [234]$) of the FIB lamella as presented here. However, their finding on stress-induced ferritic transformation was based on a Ga⁺ beam aligned parallel to the parent FCC surface normal, while it was orthogonal to our lamella surface normal.

Based on their findings, one could first speculate that the signal observed in the SADPs found around $1/3\{112\}_{\text{FCC}}$ in Figure 3a and 4 comes from a partly transformed ferrite triggered by Ga⁺ implantation. The nanometric structural modulation reflected by the streaking in the diffraction patterns and measured to be ≈ 20 nm could then be associated to an oscillation of similar frequency in the chemical composition within the cell cores. These regions could be locally enriched with other ferrite stabilizers such as Cr and Mo or Si and are transformed with even small additions of Ga⁺, while other regions with a depletion of these elements remain austenitic. This would explain why we have strong reflections from the austenite and streaked weaker reflections out of the expected FCC symmetry. Otherwise, the only other explanation of such streaks is the presence of planar defects such as the nanotwins observed in mechanically loaded specimens as reported by Barkia et al.^[22] However, no evidence was found for planar defects in any of the regions of the TEM lamella. In our case, the DFTEM images of Figure 3a and 4 show a continuous contrast for the entirety of the cell cores and MPB, which is different to a strong localization of contrast present where planar defects discretely appear.

While there is one strong streak direction (elongated toward $(01\bar{1})_{\text{FCC}}$), the two other weaker streaks could be further ferritic variants equivalent to the strongest. Since the FIB lamella has n close to $[122]_{\text{FCC}}$, it is likely that the ferritic transformation extends beyond the Ga⁺ implantation depth, which may indicate the presence of a strain-induced ferritic transformation, as suggested by Babu et al.^[50] The additional faint diffraction reflections that could be indexed as a BCC (ferrite) phase may also be the result of Ga⁺-assisted ferrite formation aided by $n \approx [122]$ and some local strain field.

The other source of streaking were the small particles (≈ 25 nm) found at some locations. However, these nanoparticles have been reported several times in literature without mentioning such diffraction effects. They have been identified here as Mn and Si containing oxides related to the PBF process.^[34] This explanation corresponds to the observed dark grey circles in the dark-field scanning transmission electron microscope (DFSTEM) image in Figure 5 and EDX analysis made on similar particles of the material investigated here (not shown). However, the streaking along $\{211\}_{\text{FCC}}$ and projected shapes found in Figure 4f could point to composite particles with core-shell structures.

Returning to the metallurgically relevant effect of a deeper etching at the MPB, Godec et al. found a depletion of Mo and

Cr at the MPB with respect to the dislocation cell wall, without a clear change in cell growth direction.^[10] The deep etching effect occurring at the MPB could therefore be attributed in an analogous manner to the etching out of isolated cell cores. However, at the MPB, the extent of the etched notch is deeper due to the equally deeper morphological feature that characterizes it. This rationale would explain why MPBs with heterogeneous thickness and depth may arise the on electropolished or etched metallographic surfaces, depending on the angle formed between the sample surface plane and the curved MPB.

The MPBs in 316 L L-PBF can be observed with light microscopy and SEM using chemical etching due to differences in the compositions compared to adjacent material.^[10] In the case observed here, the MPBs are considered to have the same composition as the cores of cells. The MPB displays cell core-like material forming a contour region and exhibiting a varying width. This contour might be formed either by the change of cell growth directions at MPBs or due to a change of solidification mode from planar to cellular. The latter case was observed for the same alloy,^[15] but to a larger amount (planar growth ≈ 3 μm in width) compared to that observed in this work. Pham et al.^[40] reported that the MPB widens to about 1 μm , which is similar to our observation, and they assumed this was due to a change of solidification mode. In other alloys, for example, in β -Ti metallic composites,^[44] the width of the planar growth is narrower (≈ 0.5 –1 μm); however, the nature of that cellular structure (multiphase as opposed to almost defect-free Cr-depleted cell cores and highly defected Cr-rich cell walls) might have facilitated its observation via SEM. The contour region of the MPB seen in this work, with a thickness of only ≈ 200 nm at its thinnest, could therefore only be presented clearly via targeted TEM preparation and imaging (see Figure 3a). The dotted lines in the newly solidified region of Figure 6c represent the aforementioned possibility that the MPB contour could have been built via planar-to-cellular or by growth direction change of newer cells. The images reported by Godec et al.^[10] did not clearly show the cell core-like contour, such that the compositional difference of MPB could also be caused by the relatively high cooling rates at the MPB compared to the rest of the melt pool during the solidification. In other literature, for example, Chen et al.^[47] have previously confirmed the cellular solidification mode at MPBs and that the change in growth direction by 90° of the cellular structure 100 depends on their alignment with the thermal gradient (G), in their case for a Co–Cr–Mo alloy. Chen et al. schematically showed, as we do in Figure 1c and 2a,b, that the cell morphology on the 2D sections is strongly dependent on the angle of the growth direction with respect to the section plane. They also showed that the aspect ratio is quantifiable using microscopy although the 3D nature of the cells must be considered. However, Chen et al. stated that there is no planar growth adjacent to the MPB (there named “track boundary”) even when the ratio between G and their growth velocity (V) were such that planar growth should be expected. We argue that the planar growth at MPBs is not clearly seen in Chen et al. because, as in most of the literature, it may have been etched away during preparation (cf. black stripe at MPB in Figure 4a and 8 of their contribution).^[47]

Overall, based on the presented microscopy, we agree that the observed structure could be described by the 90° rotation of the epitaxial growth direction due to alignment of the thermal gradient toward 100 that differ for either side of the melt pool. However, we argue that planar growth may indeed be present but not captured correctly by the analysis method most widely used in the literature, for example, etching of MPBs. Moreover, while the MPB targeted and analyzed here extended orthogonal to the surface of the sample where it was prepared by FIB, the shape of the melt pool and the laser path defined by the scanning strategy will produce MPBs at different angles from metallographic planes, so that extended or multiple lines such as highlighted by Godec et al. on their Figure 3^[10] can be explained through the 3D extension of the MPBs.

5. Conclusion

Several aspects of the submicron structures surrounding the MPBs of L-PBF 316 L were characterized in this paper. The focus was directed to the details of the cellular substructure and their relationship to MPBs. It was shown that the MPBs in L-PBF 316 L are not just a 2D interface of zero thickness, but it can have a thickness of at least 200 nm and it extends at an angle of up to 90° to the MPB interface, that is, it is a 3D feature. The MPBs consist of material similar to the cell cores of columnar cellular substructure within the grains, which explains the deeper etching (corrosion) behavior at MPBs locations, and why it therefore is not well described by etched metallographic studies. A mechanism is proposed that describes the finite thickness either as a planar-to-cellular transition or as an overlap between cells of different growth directions.

Both cell cores and MPBs exhibit a nanometer-scale-modulated substructure (≈ 21 nm in thickness), made visible by a common artifact of focused ion beam (FIB) milling 316 L stainless steel with high-energy Ga⁺ ions, that is, the phase transformation from austenite to ferrite at locations of the nano-modulation that can be stabilized by the implanted Ga⁺.

Acknowledgements

This research was funded by Bundesanstalt für Materialforschung und -prüfung (BAM) within the focus area Materials, project AGIL. The authors would like to acknowledge the contributions of the AGIL project members, in particular Gunther Mohr for the manufacture of the L-PBF 316L specimens, and Romeo Saliwan Neumann for EBSD acquisition. Insightful discussions with Prof. Walter Reimers, Prof. Gert Nolze, Dr. Grzegorz Cios and Dr. Alexander Evans are equally acknowledged.

Open Access funding enabled and organized by Projekt DEAL.

Conflict of Interest

The authors declare no conflict of interest.

Data Availability Statement

The data that support the findings of this study are available from the corresponding author upon reasonable request.

Keywords

additive manufacturing (AM), austenitic steel 316L, cellular structure, laser-based powder bed fusion (L-PBF), melt pool boundary (MPB), microstructural characterization, transmission electron microscopy (TEM)

Received: December 9, 2021

Revised: April 7, 2022

Published online:

- [1] I. Gibson, D. Rosen, B. Stucker, *Additive Manufacturing Technologies - 3D Printing, Rapid Prototyping, And Direct Digital Manufacturing*, Springer-Verlag, New York **2015**.
- [2] M. Schmidt, M. Merklein, D. Bourell, D. Dimitrov, T. Hausotte, K. Wegener, L. Overmeyer, F. Vollertsen, G. N. Levy, *Cirp Ann.-Manuf. Techn.* **2017**, 66, 561.
- [3] VDI 3405: 2014, *Additive Manufacturing Processes, Rapid Manufacturing - Basics, Definitions, Processes*.
- [4] DIN EN ISO/ASTM 52900: 2017, *Additive Manufacturing – General Principles – Terminology ISO/ASTM 52900:2015*.
- [5] DIN EN ISO/ASTM 52911-1: 2020, *Additive Manufacturing – Design – Part 1: LaserBased Powder Bed Fusion of Metals ISO/ASTM 529111:2019*.
- [6] S. Li, Q. S. Wei, Y. S. Shi, C. K. Chua, Z. C. Zhu, D. Q. Zhang, *J. Mater. Sci. Technol.* **2015**, 31, 946.
- [7] L. Zhong Hong, C. Chee Kai, L. Kah Fai, T. Lore, V. H. Jan, K. Jean-Pierre, presented at *Proc. 2012 Symp. on Photonics and Optoelectronics*, Shanghai, China **2012**.
- [8] I. Yadroitsev, A. Gusarov, I. Yadroitsava, I. Smurov, *J. Mater. Process. Tech.* **2010**, 210, 1624.
- [9] L. A. Ávila Calderón, B. Rehmer, S. Schriever, A. Ulbricht, L. Agudo Jácome, K. Sommer, G. Mohr, B. Skrotzki, A. Evans, *Mat. Sci. Eng. A*, **2022**, 830, 142223.
- [10] M. Z. Godec, S. Zaeferrer, B. Podgornik, M. Šinko, E. Tchernychova, *Mater. Charact.* **2020**, 160, 110074.
- [11] N. T. Aboulkhair, N. M. Everitt, I. Maskery, I. Ashcroft, C. Tuck, *MRS Bull.* **2017**, 42, 311.
- [12] T. DeRoy, H. L. Wei, J. S. Zuback, T. Mukherjee, J. W. Elmer, J. O. Milewski, A. M. Beese, A. Wilson-Heid, A. De, W. Zhang, *Prog. Mater. Sci.* **2018**, 92, 112.
- [13] W. M. Tucho, V. H. Lysne, H. Austbo, A. Sjolyst-Kverneland, V. Hansen, *J. Alloy Compd.* **2018**, 740, 910.
- [14] F. Y. Yan, W. Xiong, E. J. Faierson, *Materials.* **2017**, 10, 1260.
- [15] D. Wang, C. H. Song, Y. Q. Yang, Y. C. Bai, *Mater. Design.* **2016**, 100, 291.
- [16] Z. J. Sun, X. P. Tan, S. B. Tor, W. Y. Yeong, *Mater. Design.* **2016**, 104, 197.
- [17] S. Kou, in *Welding Metallurgy*, John Wiley & Sons, Hoboken, NJ **2003**, Ch. 8.
- [18] D. N. Lee, K. H. Kim, Y. G. Lee, C. H. Choi, *Mater. Chem. Phys.* **1997**, 47, 154.
- [19] C. Körner, M. Markl, J. A. Koepf, *Metall. Mater. Trans. A.* **2020**, 51, 4970.
- [20] D. C. Kong, X. Q. Ni, C. F. Dong, X. W. Lei, L. Zhang, C. Man, J. Z. Yao, X. Q. Cheng, X. G. Li, *Mater. Design.* **2018**, 152, 88.
- [21] K. M. Bertsch, G. M. de Bellefon, B. Kuehl, D. J. Thoma, *Acta Mater.* **2020**, 199, 19.
- [22] B. Barkia, P. Aubry, P. Haghi-Ashtiani, T. Auger, L. Gosmain, F. Schuster, H. Maskrot, *J. Mater. Sci. Technol.* **2020**, 41, 209.
- [23] J. C. Simmons, X. B. Chen, A. Azizi, M. A. Daeumer, P. Y. Zavalij, G. W. Zhou, S. N. Schiffres, *Addit. Manuf.* **2020**, 32, 100996.

- [24] K. Saeidi, X. Gao, F. Lofaj, L. Kvetkova, Z. J. Shen, *J. Alloy Compd.* **2015**, 633, 463.
- [25] X. Q. Ni, D. C. Kong, W. H. Wu, L. Zhang, C. F. Dong, B. B. He, L. Lu, K. Q. Wu, D. X. Zhu, *J. Mater. Eng. Perform.* **2018**, 27, 3667.
- [26] P. Krakhmalev, G. Fredriksson, K. Svensson, I. Yadroitsev, I. Yadroitsava, M. Thuvander, R. Peng, *Metals.* **2018**, 8, 643.
- [27] K. Akino, K. Kakehi, *Mater. Trans.* **2018**, 59, 482.
- [28] K. O. Bazaleeva, E. V. Tsvetkova, E. V. Balakirev, I. A. Yadroitsev, I. Y. Smurov, *Russ. Metall.* **2016**, 2016, 424.
- [29] P. Krakhmalev, I. Yadroitsava, G. Fredriksson, I. Yadroitsev, *S. Afr. J. Ind. Eng.* **2017**, 28, 12.
- [30] S. Leuders, T. Lieneke, S. Lammers, T. Troster, T. Niendorf, *J. Mater. Res.* **2014**, 29, 1911.
- [31] C. Man, Z. W. Duan, Z. Y. Cui, C. F. Dong, D. C. Kong, T. T. Liu, S. G. Chen, X. Wang, *Mater. Lett.* **2019**, 243, 157.
- [32] J. Man, K. Obrtlík, M. Petreñec, P. Beran, M. Smaga, A. Weidner, J. Dluhos, T. Kruml, H. Biermann, D. Eifler, J. Polak, *Procedia Eng.* **2011**, 10, 1279.
- [33] A. H. Puichaud, C. Flament, A. Chniouel, F. Lomello, E. Rouesne, P. F. Giroux, H. Maskrot, F. Schuster, J. L. Bechade, *EPJ Nucl. Sci. Technol.* **2019**, 5, 23.
- [34] C. Qiu, M. A. Kindi, A. S. Aladawi, I. A. Hatmi, *Sci. Rep.* **2018**, 8, 7785.
- [35] O. O. Salman, C. Gammer, A. K. Chaubey, J. Eckert, S. Scudino, *Mat. Sci. Eng. A.* **2019**, 748, 205.
- [36] Z. J. Sun, X. P. Tan, S. B. Tor, C. K. Chua, *NPG Asia Mater.* **2018**, 10, 127.
- [37] D. C. Kong, C. F. Dong, S. L. Wei, X. Q. Ni, L. Zhang, R. X. Li, L. Wang, C. Man, X. G. Li, *Addit. Manuf.* **2021**, 38, 101804.
- [38] K. Saedi, X. Gao, Y. Zhong, Z. J. Shen, *Mater. Sci. Eng. A-Struct.* **2015**, 625, 221.
- [39] G. Mohr, S. J. Altenburg, K. Hilgenberg, *Addit. Manuf.* **2020**, 32, 101080.
- [40] M. S. Pham, B. Dovggy, P. A. Hooper, C. M. Gourlay, A. Piglione, *Nat. Commun.* **2020**, 11, 749.
- [41] C. C. Zhang, H. H. Zhu, Z. H. Hu, L. Zhang, X. Y. Zeng, *Mater. Sci. Eng. A.* **2019**, 746, 416.
- [42] K. V. Yang, Y. J. Shi, F. Palm, X. H. Wu, P. Rometsch, *Scripta Mater.* **2018**, 145, 113.
- [43] J. P. Choi, G. H. Shin, S. Yang, D. Y. Yang, J. S. Lee, M. Brochu, J. H. Yu, *Powder Technol.* **2017**, 310, 60.
- [44] B. Vrancken, L. Thijs, J. P. Kruth, J. Van Humbeeck, *Acta Mater.* **2014**, 68, 150.
- [45] G. Mohr, K. Sommer, T. Knobloch, S. J. Altenburg, S. Recknagel, D. Bettge, K. Hilgenberg, *Metals.* **2021**, 11, 1063.
- [46] ASTM A276/A276M-17: 2017, *Standard Specification for Stainless Steel Bars and Shapes.*
- [47] Z. W. Chen, M. A. L. Phan, K. Darvish, *J. Mater. Sci.* **2017**, 52, 7415.
- [48] K. Knipling, D. J. Rowenhorst, R. Fonda, G. Spanos, *Mater. Charact.* **2010**, 61, 1.
- [49] A. Basa, C. Thaulow, A. Barnoush, *Metall. Mater. Trans. A.* **2014**, 45, 1189.
- [50] P. B. Revathy Rajan, S. Irukuvarghula, A. Harte, M. Preuss, *Acta Mater.* **2016**, 120, 391.
- [51] J. Li, P. Liu, in *Characterization Of Minerals, Metals, And Materials* (Eds.: J. Li et al.), Springer, Cham, **2020**, Ch. 8.
- [52] E. J. Seo, L. Cho, J.-K. Kim, J. Mola, L. Zhao, S. Lee, B. De Cooman, *J. Alloys Compd.* **2019**, 812, 152061.